



Corner states in photonic higher-order Dirac semimetals

José A. Medina-Vázquez ^{*}, Evelyn Y. González-Ramírez, and José G. Murillo-Ramírez 
*Centro de Investigación en Materiales Avanzados S.C., Complejo Industrial Chihuahua, Miguel de Cervantes 120,
 C.P. 31136, Chihuahua, México*



(Received 22 December 2022; revised 9 April 2023; accepted 1 May 2023; published 12 May 2023)

The introduction of higher-order topological insulators featuring topological corner states has been an extremely active topic for the generation of confined modes. Recent studies show that corner states are not an exclusive feature of topological insulators but can also exist as bound states in the continuum (BIC). This suggests that corner states may exist in different topological phases that exhibit a higher-order character, beyond the conventional bulk-edge correspondence. In this paper, we show that corner states can appear in a higher-order Dirac semimetal phase of a two-dimensional photonic lattice. Such a lattice displays a dispersion relationship with a fourfold degeneracy, which serves to induce a higher-order topological phase transition, leaving a Dirac point between two edge bands. Just as Dirac modes exist in regular lattice defects, the nonconventional bulk-edge-corner correspondence leads to corner states in the Dirac semimetal phase. Notably, the induced corner state exhibits an algebraic decay characteristic of long-range interactions, predicted by the massless Dirac equation. The analysis of the field profile and quality factors indicates that the state is not a BIC, but rather a corner-Dirac state. We show that if the photonic lattice does not present a higher-order phase transition the existence of the corner-Dirac state does not arise. The results obtained in this paper indicate that corner states can exist throughout the entire topological phase transition process, even in the semimetal phase, and pave the way to generate light-matter interactions with such a photonic bath.

DOI: [10.1103/PhysRevA.107.053511](https://doi.org/10.1103/PhysRevA.107.053511)

I. INTRODUCTION

Since the discovery of the extraordinary electronic properties of graphene, Dirac materials have been the subject of extensive studies. This has triggered a search to find a Dirac energy spectrum in other systems, such as photonic crystals (PhC), exploiting the similarities between the propagation of electronic and electromagnetic waves [1–6]. PhCs have played a key role in developing optical nanocavities, conceiving the strongest concentration of light in all-dielectric materials [7–13]. Such PhC cavities can achieve quality factors (Q) exceeding 1×10^6 in volumes of the order of a cubic wavelength [13–17]. Similarly, PhC cavity slabs, formed by the absence of holes in a dielectric medium, confer enormous capacities for on-chip integration. In addition, PhC cavities facilitate the fundamental study of light-matter interaction by integrating quantum emitters, such as quantum dots, which lie at the core of cavity quantum electrodynamics [18].

On the other hand, in recent years, topological systems have attracted immense attention in various disciplines [19–22]. Subsequently, the existence of higher-order topological insulators (HOTIs) was predicted [23–26] and then observed experimentally [27–29]. In this new class of materials, their symmetries lead to the formation of topological phases that shield localized corner states with zero dimensionality. More generally, HOTIs admit states with dimensionality ($D - n$) with $n \geq 2$, at the boundaries of two different topologies of a lattice with dimensionality D [30–44]. In this

sense, HOTIs extend the earlier knowledge about topological insulators. The robust features offered by HOTIs enable the development of photonic crystal nanocavities and low-threshold corner-state lasers, among many other applications [45,46]. Furthermore, the crystal symmetries that shield the topological phases do not necessarily require the existence of a bulk band gap [47,48]. This conclusion quickly raised a question regarding the existence of corner states that remain confined despite being degenerate in the bulk band continuum. Hence, addressing this question, the connection between HOTIs and bound states in the continuum (BIC) has been explored [47–49].

Besides BICs, the so-called Dirac modes are other types of states that degenerate into the bulk band continuum and remain confined to a particular volume [50–53]. In this case, the confinement is due to the vanishing density of states (DOS) at the Dirac points, where is found the Dirac mode frequency. The emergence of Dirac modes in regular photonic lattices occurs in the presence of structural defects, and when the resonant frequency of the defect coincides with the Dirac frequency it becomes a Dirac mode. In particular, the Dirac modes exhibit an algebraic decay predicted by the massless Dirac equation, where such waves are singular at a propagation distance equal to zero [50]. Thus, Dirac modes cannot exist in infinite lattices, only in finite ones with some sort of defect. A fascinating feature recently studied in Dirac photonics is the possibility of obtaining decoherence-free, power-law interaction between emitters [54,55].

In topological systems, Dirac points on band diagrams indicate an imminent topological phase transition by opening a band gap and achieving the higher-order topological (HOT)

^{*}Corresponding author: jose.medina@cimav.edu.mx

phase. Recently, Dirac semimetal (DSM) phases have entered the field of HOT phases by separating the normal insulating phase and the HOTI phase only by a Dirac point, achieving a higher-order Dirac semimetal (HODSM) phase [56–63]. Despite all the recently gained knowledge, the physics behind Dirac points in the DSM phase is still very rich and represents a promising way to find new topological confined states even if there is no band gap. For example, it was recently shown that with a symmetry mismatch between a very well-tuned defect mode and the Bloch modes of a typical PhC a BIC is attainable in a point defect at the Dirac point frequency [64].

In this paper, we demonstrated the existence of a corner state in the HODSM phase of a two-dimensional (2D) photonic crystal that mimics an extended two-dimensional Su-Schrieffer-Heeger (SSH) model. The HODSM phase can be induced from a fourfold degeneracy, which is then lifted, leaving a Dirac point accompanied by two edge bands. Next, we find a corner state at the frequency of the Dirac point localized on the photonic band diagram and at the topological corner of the photonic lattice. We confirm that this corner mode is indeed a Dirac mode due to its spectral location and exhibits a characteristic algebraic decay described by the massless Dirac equation. Additionally, in this paper it was also found that a defect located at the center of the topological PhC significantly improves the confinement of the mode without losing the characteristics of the Dirac mode. Hence, we coin this state as a corner-Dirac mode existing at a HODSM phase. Finally, we show that the corner-Dirac state disappears if the photonic lattice loses its higher-order topology, which we demonstrated by studying a first-order topological model that only fulfills the conventional bulk-edge correspondence. These results extend our knowledge about the existence of confined corner states in topological systems that exhibit topological phase transitions and provide an alternative to generate exotic confined light modes.

II. CHARACTERIZATION OF THE HIGHER-ORDER DIRAC SEMIMETAL PHASE

In order to obtain a structure that displays higher-order topological features, we rely on a simple case such as a PhC slab with square lattice and square air holes, with the C_4v point-group symmetry. The unit cell describing the initial state of the system is shown in Fig. 1(a), where the four holes are separated by a distance L , and placed on a GaAs slab for practical purposes. Here, the lattice parameter of the PhC is a , while the side of the holes is $0.32a$. Subsequently, the process to generate the topological phase transition consists of expanding and shrinking the structural parameters of the unit cell in a symmetrical manner. This process results in the formation of two unit cells (UC1 and UC2), as shown in Fig. 1(b). Here we use first-principles calculations to rigorously analyze the system and obtain all the topological phenomena that may arise in our topological photonic system.

Following the methodology mentioned above, we obtained the photonic band diagrams by the finite element method, using the COMSOL software employing the eigenfrequency resolver. For simplicity, the band diagram was calculated using a 2D effective model with an effective dielectric constant $\epsilon_{\text{eff}} = 8.631$ of a GaAs slab with a thickness $t =$

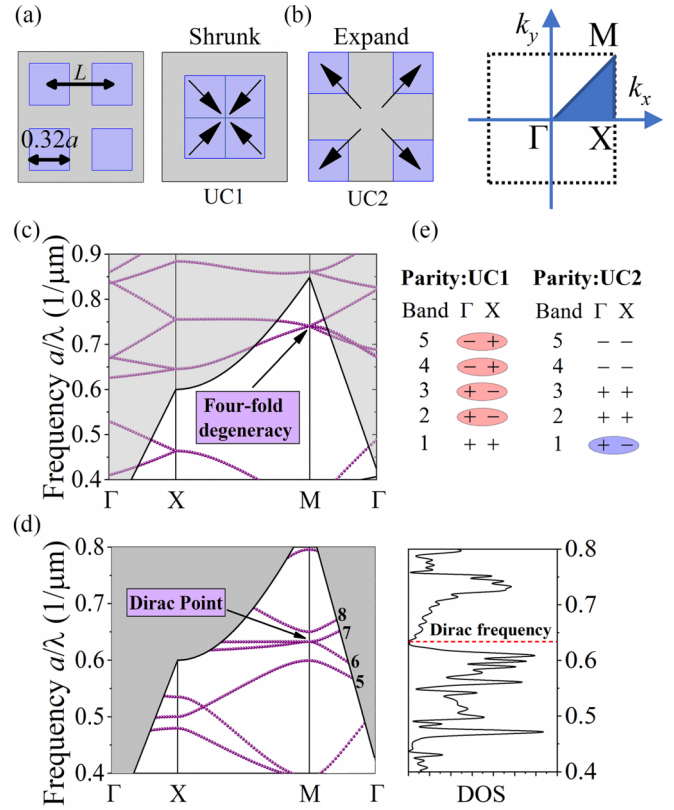


FIG. 1. (a) Original unit cell that can be described by the Hamiltonian of Eq. (1). Each unit cell contains four identical air holes. (b) The shrinking and expanding of the structural parameters form the unit cells UC1 and UC2, which exhibit a topological phase transition. Illustrated to the right is the path of the k -wave vectors through the unit cells. (c) Photonic band diagram, corresponding to the unit cell shown in (a), and displaying a fourfold degeneracy formed with bands 5 to 8 at the high-symmetry point M . (d) Corresponding photonic band diagram to UC1 and UC2, showing the lifted degeneracy and the presence of a Dirac point between bands 6 and 7 at point M . At the right is the related density of states, showing the Dirac frequency where the density of states vanishes. (e) Parities of the first five photonic bands below the Dirac point and the edge bands at gamma and X for UC1 and UC2, respectively.

0.535 a . We consider the harmonic TE modes of an electromagnetic wave, namely, those of finite out-of-plane H_z and in-plane E_x and E_y components with others being zero, in a dielectric medium. The master equation for the harmonic mode with frequency ω is derived from Maxwell's equations [22], $[\nabla^2 + (\omega^2/c^2)\epsilon(\mathbf{r})]\mathbf{E} = 0$ where $\epsilon(\mathbf{r})$ is the position-dependent permittivity and c is the speed of light. The Faraday relation gives the magnetic field $\mathbf{H} = -[i/\mu_0\omega]\nabla \times \mathbf{E}$, where the permeability μ_0 is that of the vacuum. Next, we impose periodic boundary conditions at the boundaries perpendicular to the plane of the unit cell.

The photonic band diagram of the original unit cell [Fig. 1(a)] is shown in Fig. 1(c). This band diagram was used as a reference to find a phase transition when expanding and shrinking the structural parameters of the unitary cell. Importantly, this band diagram shows a fourfold degeneracy between bands 5 through 8, thus representing a rich system

for generating higher-order topological effects. Figure 1(d) shows the photonic band diagram for the UC1 and UC2, which is certainly identical for both unit cells. In this last band diagram, the fourfold degeneracy is lifted for bands 5 to 8, which leaves only a Dirac point between bands 6 and 7 at the M high-symmetry point. The photonic DOS, also shown in Fig. 1(d), is given by

$$D(\omega) = \sum_n \int_{\mathbf{k} \in \text{BZ}} \delta[\omega - \omega_n(\mathbf{k})] d\mathbf{k}, \quad (1)$$

where $\omega_n(\mathbf{k})$ is the angular frequency eigenvalue for the momentum values \mathbf{k} within the Brillouin zone (BZ), and n is the band index. Indeed, it is observed that the DOS vanishes around the Dirac point until they reduce to zero. This vanishing DOS implies that effective suppression of radiation losses is achieved at the Dirac point and enables the formation of a Dirac mode at that frequency.

To characterize the topological phase transitions, it is required to calculate the topological invariant. Here, the relevant topological invariant is the 2D Zak phase or 2D polarization \mathbf{P} , defined as the integral of the Berry connection taken over the first Brillouin zone [22,49]:

$$\mathbf{P} = \frac{1}{2\pi} \int_{\text{BZ}} dk_x dk_y \text{Tr}[A_\alpha(k_x, k_y)], \quad (2)$$

where $A_\alpha(k_x, k_y) = i\langle \psi_\alpha | \partial_{\mathbf{k}} | \psi_\alpha \rangle$ is the Berry connection, $|\psi_\alpha\rangle$ represents the periodic parts of the Bloch function, and α represents the band index. Similar to Refs. [48,49,65], we determine the topological properties of the system by analyzing the bulk bands that lie below the photonic bands where occurs the Dirac point, i.e., from band 1 to band 5. It is important to remark that the 2D Zak phase of a system without a band gap conventionally cannot be rigorously defined. However, as the phase transition occurs from band 5 to band 8, the dipole moment \mathbf{P} is in the fifth and eighth bands and can be well defined since they are gapped [40,48]. This dipole moment is accompanied by two bands (6 and 7) with edge states spectrally isolated from the bulk bands, originating the DSM phase. The proposed topological phase transition induced in four bands leaving an isolated Dirac point is a different alternative compared to the methodologies already studied to generate HODSM phases [62,63].

Our system presents inversion symmetry, so \mathbf{P} is quantized, and the calculation is substantially simplified. Applying group theory, one finds that the values of the quantization can only take values of 0 and 1/2, determined only by the parity of the bulk states at the points of high symmetry in the first Brillouin zone, and given by [49,65]

$$P_m = \frac{1}{2} \left(\sum_\alpha q_m^\alpha \text{mod} 2 \right), \quad (-1)^{q_m^\alpha} = \frac{\eta(X_m)}{\eta(\Gamma)}, \quad (3)$$

where the summation is taken over all occupied bands, η denotes the parity with π rotation, and m stands for x or y . Equation (3) implies a simple rule to identify the topological properties of the system through the number of pairs of parities with opposite signs in Γ and X for the same band. In other words, an odd number of opposite parities indicates the nontrivial topology, while an even number indicates the trivial topology. The corresponding profiles of the eigenmodes used

to identify the parities of the bands are shown in the Appendix A. Figure 1(e) shows the results of the parities obtained at the high-symmetry points Γ and X for the UC1 and UC2 corresponding to bands 1 to 5. Here, a minus sign represents odd parity, while a plus sign is even parity. Then, taking the results of Fig. 1(e) into Eq. (3), it can be determined that the UC2 is in the nontrivial topological phase with $\mathbf{P} = (1/2, 1/2)$, while the UC1 is in the trivial phase with $\mathbf{P} = (0, 0)$. Note that, as the photonic lattice has C_{4v} symmetry, $P_x = P_y$. These results, together with those obtained through DOS, indicate that the system is in the HODSM phase.

Although we have shown that the proposed photonic model has higher-order topological features, it would be illustrative to describe in a general way the topological system through a tight-binding model. In this way, we can demonstrate that long-range interactions (LRIs) are responsible for the shape and characteristics of the band structure in our model. Typically, the SSH model is used to induce higher-order topological phase transitions [24,48,49]. In photonic systems, it has been studied that the SSH model predicts, to some extent, the higher-order topological phase transition [48,49]. However, the conventional SSH model does not include LRIs, which are intrinsically present in photonic systems. For this reason, the conventional SSH model does not accurately reproduce the photonic band structure, making it difficult to explain phenomena occurring in the LRI regime. Therefore, we propose an extended Hamiltonian of the SSH model, including LRI by adding next-nearest-neighbor (NNN) couplings. The extended Hamiltonian is described by

$$H = H_0 + H_{\text{NNN}} \quad (4)$$

where H_0 represents the coupling Hamiltonian between the nearest neighbors (NNs) and the intracellular NNNs. Meanwhile, H_{NNN} is the coupling Hamiltonian between the remaining NNNs. The matrix representation of H_0 is given by

$$H_0 = \begin{pmatrix} 0 & t_1 + t_2 e^{-ik_x} & t_1 + t_2 e^{ik_y} & t_3 e^{-ik_x + ik_y} \\ t_1 + t_2 e^{ik_x} & 0 & t_3 e^{ik_x + ik_y} & t_1 + t_2 e^{ik_y} \\ t_1 + t_2 e^{-ik_y} & t_3 e^{-ik_x - ik_y} & 0 & t_1 + t_2 e^{-ik_x} \\ t_3 e^{ik_x - ik_y} & t_1 + t_2 e^{-ik_y} & t_1 + t_2 e^{ik_x} & 0 \end{pmatrix} \quad (5)$$

where t_1 and t_2 are the hopping between the inter- and intracellular NNs, respectively, and t_3 is the hopping between the intracellular NNNs. Then, the matrix representation of H_{NNN} is

$$H_{\text{NNN}} = \begin{pmatrix} 0 & 0 & 0 & h_1 \\ 0 & 0 & h_2 & 0 \\ 0 & h_2^* & 0 & 0 \\ h_1^* & 0 & 0 & 0 \end{pmatrix} \quad (6)$$

with the matrix elements

$$h_1 = t_4 e^{ik_x - ik_y} + t_5 (e^{ik_x + ik_y} + e^{-ik_x - ik_y}),$$

$$h_2 = t_4 e^{-ik_x - ik_y} + t_5 (e^{-ik_x + ik_y} + e^{ik_x - ik_y}). \quad (7)$$

Here, t_4 and t_5 are the hopping terms between the remaining NNNs. The proposed model is visualized in Fig. 2(a), indicating all the hopping terms. Through this tight-binding model,

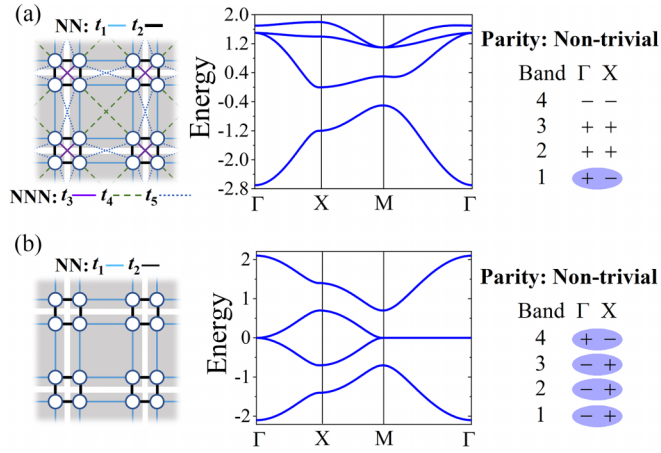


FIG. 2. (a) Schematization of the tight-binding model described by the Hamiltonian of Eq. (4). Here, t_1 and t_2 are the hopping terms of the coupling between NNs with values of 0.35 and 1, respectively. t_3 , t_4 , and t_5 are the hopping terms of the coupling between NNNs with values of 0.9, 0.2, and 0.1, respectively. The middle panel shows the band structure of the proposed tight-binding model, while the band parities at the high-symmetry points are shown on the right. (b) Schematization of a 2D SSH model with the absence of coupling between NNNs. In the center is shown the band structure of the SSH model with their respective parities at the high-symmetry points on the right.

we obtained a band structure where an appropriate tuning of the amplitude of the hopping terms leads to a remarkable coincidence with the band structure of the photonic model [see Fig. 9(a) in Appendix A]. It is important to point out that the tight-binding model we propose only has four sites per unit cell, so it can only be compared with the first four bands of the photonic model. Subsequently, the calculation of the band parities indicates an agreement with the band parities of the photonic model, demonstrating that the topological properties of the systems are equivalent. On the other hand, we compare the results obtained by our Hamiltonian with a conventional SSH Hamiltonian. We find that the absence of LRI in the SSH model does not lead to a reasonable comparison with the band structure of the photonic model. The results obtained from the SSH Hamiltonian are shown in Fig. 2(b), confirming that the presence of the LRIs manifested through couplings between NNNs gives rise to the band structure of the photonic model that we proposed.

III. CORNER STATES IN THE HODSM PHASE

Unit cells UC1 and UC2 constitute two topologically distinct PhCs; in view of this, we proceeded with the design of a topological cavity formed by the intersection of the two PhCs. The resulting structure is shown in Fig. 3(a). We point out that the design of the proposed structure has a bowtie-type architecture [66], which has been shown to have remarkable confinement capabilities. By separating the nontrivial topological quadrants [right panel of Fig. 3(a)], it is possible to tune the confinement and the frequencies of corner states that arise within the topological bowtie cavity (TBC). This approach gives the photonic structure a simple degree of

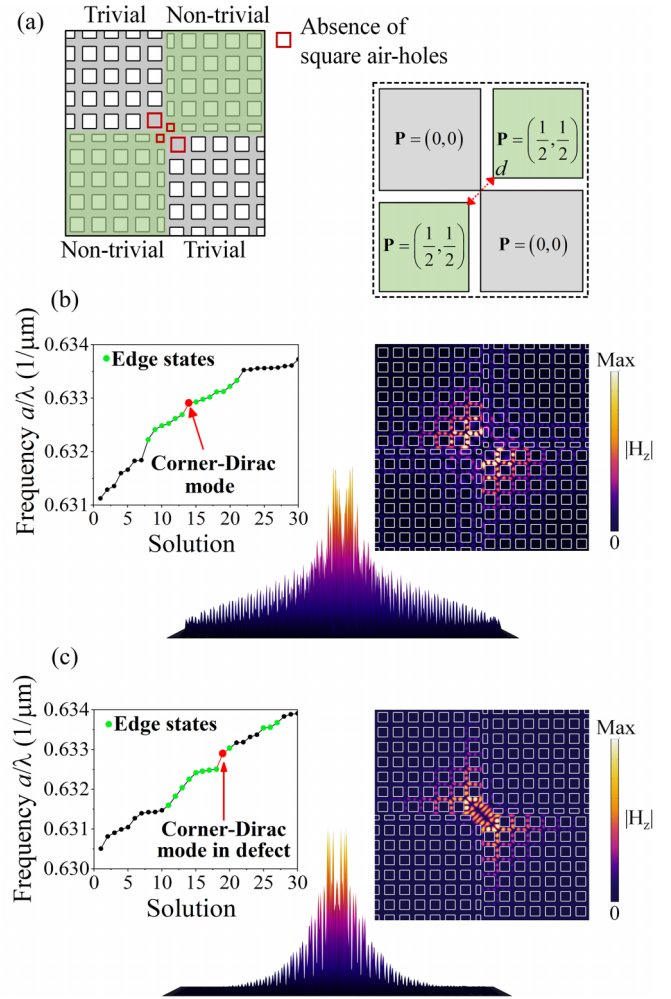


FIG. 3. (a) Illustration of the formation of the TBC composed of trivial and nontrivial lattices. A structural defect is formed by the absence of the air holes located at the corner of each net and highlighted in red. On the right, the values of the 2D polarization presented by each quadrant are shown, in addition to the separation d used to optimize the frequency of the resonant mode. (b) Solutions of the eigenfrequencies obtained near the Dirac frequency and the location of a corner-Dirac mode. Also shown is the corner-Dirac mode field distribution and a height plot. (c) Solutions of the eigenfrequencies obtained near the Dirac frequency and the location of the corner-Dirac mode in the TBC now with the structural defect shown in (a). In addition, we show the distribution of the corner-Dirac mode field and a height plot indicating a narrower field profile.

freedom to alter the properties of the modes induced in the central structural defect. Moreover, this type of configuration presents the typical 90° corner that separates the two types of topologies, so a topological corner charge based on the 2D polarization is obtained as [22,49]

$$Q^c = 4P_x P_y. \quad (8)$$

As a result, the corner charge on the TBC in the HODSM phase is $Q^c = 1$.

Figure 3(b) shows the calculated eigenfrequencies near the Dirac point and the field distribution of the corner Dirac mode located at the center of the TBC. Immediately, we note that the spatial distribution of the mode, for the most part, does not lie in the region of the nontrivial topological quadrant. This may be counterintuitive; nevertheless, several works have reported that the corner state may be strongly localized in the trivial phase of the PhC topology, especially when it is a type-II corner state [67]. In this type of corner state, the bulk-edge-corner correspondence is the dominant origin of corner states, causing delocalized and spread modes. Furthermore, type-II corner states appear when considering interactions beyond NNN. As Dirac modes appear due to LRI, the corner modes found in this paper are expected to have a large modal volume, and it is not unusual to be located relatively outside the nontrivial quadrant. However, the corner-Dirac state should not be confused with a type-II corner state because the latter is only found in insulating topological phases. Here, we only point out their similarities in the nature of their field profiles originating from LRIs. Later we confirm this hypothesis using a lattice that does not have a higher-order topology. In Appendix B, we have verified that the corner-Dirac mode exists in a more usual configuration, similar to that found in the literature [22], confirming that its existence is not due to the TBC configuration.

In order to demonstrate the versatility of the corner-Dirac mode, we introduced a structural defect in the center of the TBC. This approach also serves to inspect the robustness of the corner-Dirac mode against disturbances. We point out that a structural defect located at the topological corner of the TBC can support corner states in the HOTI phase. This study is also presented in Appendix C and provides a background to analyze the Dirac-corner mode in the structural defect. Figure 3(a) shows the considered structural defect, which consists of the absence of air holes highlighted in red. The eigenfrequencies found close to the Dirac frequency for the TBC with the added defect are shown in Fig. 3(c). Here, we note that the frequency does not present a significant change regarding the case without defects, showing that the corner-Dirac state exhibits good robustness against severe perturbations. Moreover, the field distribution and a height plot help evaluate the corner state confinement. The height plot shows that the optical confinement is significantly improved, presenting a narrower field profile. This result is quite interesting since, intuitively, one can presume that, being topologically robust, the corner state confinement would not be strongly affected by the structural defect. However, conventional Dirac modes exist inherently in structural defects of regular lattices; hence the introduced defect in the TBC also addresses the confinement of the corner-Dirac mode. This result shows that virtues of both the corner states and the Dirac mode in the studied system are effectively combined.

As mentioned, topological corner states result from edge-corner correspondence in higher-order topological systems. In this sense, we calculate the local density of states (LDOS) in the TBC and observe the edge states close to the Dirac-corner mode. This calculation also serves to justify the hypothesis formulated about the edge bands that form the Dirac point in the photonic band diagram. We calculate the LDOS using the finite difference time-dependent method (FDTD). By

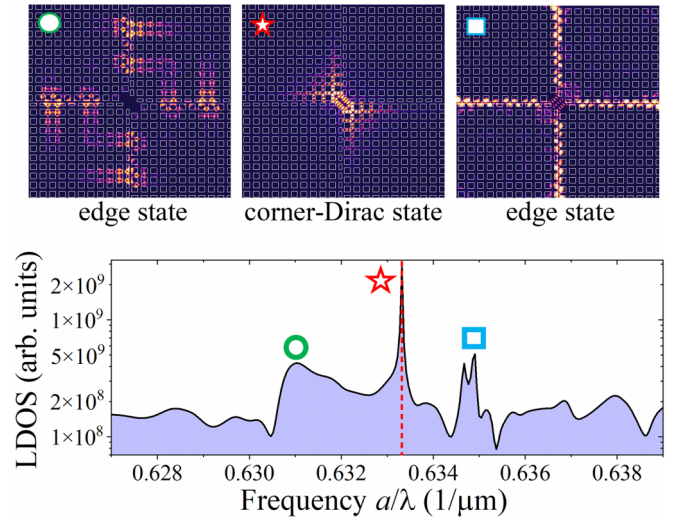


FIG. 4. Characterization of the model described by the TBC. The lower panel shows the LDOS obtained from accumulating the Fourier transform in the time domain of the field at a point in real space at the center of the TBC. The top panel shows the edge states and the corner-Dirac mode, which we label respectively with a circle, square, and star in the LDOS. The two broad peaks that delimit the corner-Dirac mode correspond to the edge states found in the photonic bands 6 and 7, showing that they are the edge bands. The sharp peak in the LDOS located at the Dirac frequency (dotted red line) corresponds to the corner-Dirac mode.

exciting a dipole source in the FDTD simulation, the time-domain Fourier transform of the field can be accumulated at a real-space point to obtain the LDOS spectrum in a single calculation [68]. Figure 4 shows the LDOS spectrum at the center of the TBC. The dipole excitation source was placed at a random point near the center of the structure. There is a sharp resonance mode matching the frequency of the corner-Dirac mode and two broad modes that represent the edge states in the TBC. At the top of Fig. 4, we show the field distributions corresponding to the labeled modes in the LDOS spectrum. With this result, we confirm the existence of edge states in the edge bands and their hierarchical correspondence with the corner state.

IV. ANALYSIS OF THE CORNER-DIRAC MODE AND ALGEBRAIC DECAY

Finding a resonant mode close to the Dirac frequency is not enough to meet the requirements of a Dirac mode. In addition to being at the Dirac frequency, the mode should present an algebraic decay. Consequently, modes that are close to the Dirac frequency satisfy the 2D massless Dirac equation [50–53]

$$\begin{pmatrix} 0 & -ic_D(\partial_x - i\partial_y) \\ -ic_D(\partial_x + i\partial_y) & 0 \end{pmatrix} \begin{pmatrix} \psi_1 \\ \psi_2 \end{pmatrix} = 2\pi(f - f_D) \begin{pmatrix} \psi_1 \\ \psi_2 \end{pmatrix} \quad (9)$$

where c_D represents the group velocity, f_D is the Dirac frequency, and ψ_1 and ψ_2 correspond to the envelope of the amplitudes of the two degenerate Bloch states at points M of our photonic lattice. Equation (9) yields solutions of the

form $\psi_{1,2} \propto 1/(x \pm iy)^m$ at frequency f_D . This class of modes has been previously studied for charge carriers in graphene, and the situation is similar in PhCs. Through an analysis of the general solutions of the eigenstates around the M points and the modulation from plane waves to cylindrical waves, the solutions for the PhC at the Dirac frequency are $H_z \propto r^{-m} J_l(Mr) e^{\pm i(l-m)\theta}$, where J_l is a Bessel function of order l and r represents the propagation distance. We can approximate $J_l(Mr) \approx 2(2\pi Mr)^{-1/2} \cos(Mr - \pi/4 - l\pi/2)$ if the argument (Mr) becomes large. In this regard, it is evident that there is a wave solution, whose envelope amplitude decays algebraically for large values of r , with the form $1/r^{m+1/2}$. This results in the emergence of wave localization at the Dirac frequency in the proposed PhC, confirming the algebraic profile of the mode [50,55]. This type of wave cannot exist in infinite PhCs because they are singular at $r = 0$. However, these can exist localized in a PhC defect. Here, we argue that the filling anomaly and the symmetries that give rise to a HOT corner state can serve as mechanisms to produce Dirac mode localization. This is due to the fact that the zero-dimensional corner states are the photonic analogs of the states responsible for the filling anomalies and fractional charges in electronic systems [69]. Thus, the corner state predicted through Eq. (8) implicitly suggests the presence of the filling anomaly [40]. Therefore, due to the absence of structural defects in the proposed photonic structure, the only mechanism that can give rise to a Dirac mode, in our photonic system, is the filling anomaly related to the nonzero corner charge.

According to the solutions of Eq. (9), the corner-Dirac mode located at the Dirac frequency must satisfy an algebraic decay as $1/r^{m+1/2}$. In this regard, we extract the cross section of the amplitude envelope of the corner states at the Dirac frequency. Next, we plot the product of the modulus of the H_z field component with the factor $r^{m+1/2}$, where m takes the value of 1. The results are shown in Fig. 5(a) for the corner mode with no defect and in Fig. 5(b) for the corner mode with the localized defect. As a result, we observe an amplitude that remains constant in the mode tails as the propagation distance r increases. This behavior indicates that the corner states both with and without the defect found at the Dirac frequency exhibit algebraic decay as $1/r^{3/2}$. Therefore, we unambiguously confirm that the corner states found at the Dirac frequency are corner-Dirac modes present in a HODSM phase.

Regarding the confinement of the corner-Dirac mode, we mention that the confinement is high and that the defect located in the center of the TBC improves such confinement. We prove this statement by calculating the quality factor (Q). The Q factors for both cases are depicted in Figs. 5(c) and 5(d), plotted as a function of the separation d between the nontrivial topological quadrants. This procedure also helps to elucidate the availability for tuning the corner state frequency to the Dirac frequency. As the two frequencies coincide, the maximum confinement is achieved, highlighted by the dotted line in Figs. 5(c) and 5(d). Notably, in both cases, the Q factor is remarkably high even though the decay is algebraic and not exponential like the modes confined by conventional means. In conjunction with the algebraic decay, the behavior of the Q factor indicates that the mode is indeed a Dirac mode since a

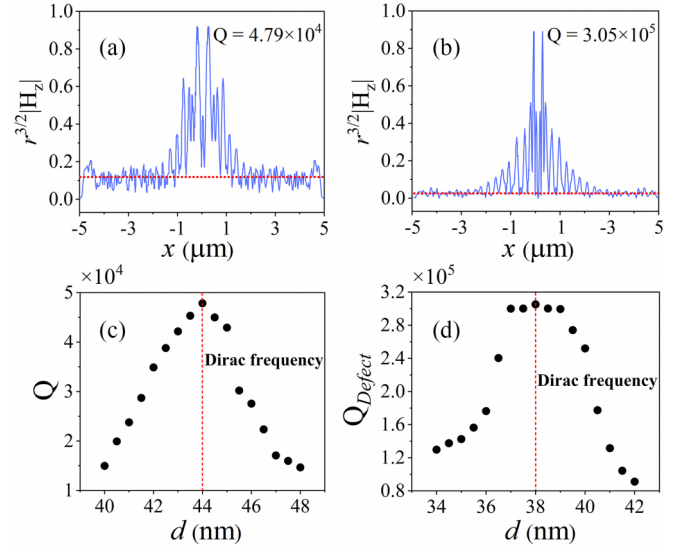


FIG. 5. (a) Product of $|H_z|$ and $r^{3/2}$ along the x axis in the TBC without the structural defect. (b) Product of $|H_z|$ and $r^{3/2}$ along the x axis in the TBC with the structural defect introduced. In both figures, a red dotted line illustrates that the tail of both products remains constant, which reveals that the mode decays algebraically as $1/r^{3/2}$. (c) Dependence of the Q factor with the separation d of the nontrivial quadrants in the TBC. The dotted line indicates the Dirac frequency, where the corner-Dirac mode with the highest Q factor value is located. (d) Dependence of the Q factor on the separation d of the nontrivial quadrants in the TBC, now with the structural defect introduced. The maximum Q value for the corner-Dirac mode is found at the Dirac frequency. The modes used in (a) and (b) have the highest Q factors found at the Dirac frequency. For this analysis, we use a lattice parameter of $a = 0.280 \mu\text{m}$ of the regular lattice composing the nontrivial and trivial quadrants.

BIC can also arise at a Dirac point [64]. However, the behavior of the Q factor of a BIC is sharply divergent, such that its maximum confinement may be difficult to achieve experimentally. Here, the behavior of the Q factor of the corner Dirac mode does not show this sharp divergence so that, together with the simplicity of the structure, it can be easily implemented experimentally.

Finally, we check that the emergence of the corner-Dirac mode in the HODSM phases does not appear in a non-higher-order configuration. The configuration of the TBC initially proposed in this paper consists of a photonic lattice with 2D polarization $\mathbf{P} = (0, 0)$ for the trivial case and $\mathbf{P} = (1/2, 1/2)$ for the nontrivial case. However, if the polarization of the nontrivial lattice is $\mathbf{P} = (0, 1/2)$, the structure should not show corner states. Thus, we set up a cavity similar to the original TBC, but now with a quadrant having a 2D polarization $\mathbf{P} = (0, 1/2)$, resulting in the structure of Fig. 6(a). When calculating the eigenfrequencies shown in Fig. 6(b), we find only edge states in the Dirac semimetal phase because of the absence of the HOT character. The result of this practice is also interesting because edge states are present in the Dirac semimetal phase, even in the absence of a band gap. Additionally, in Fig. 6(c), we calculate the eigenfrequencies of the new structure, now introducing the structural defect shown in Fig. 6(a). In this case, we

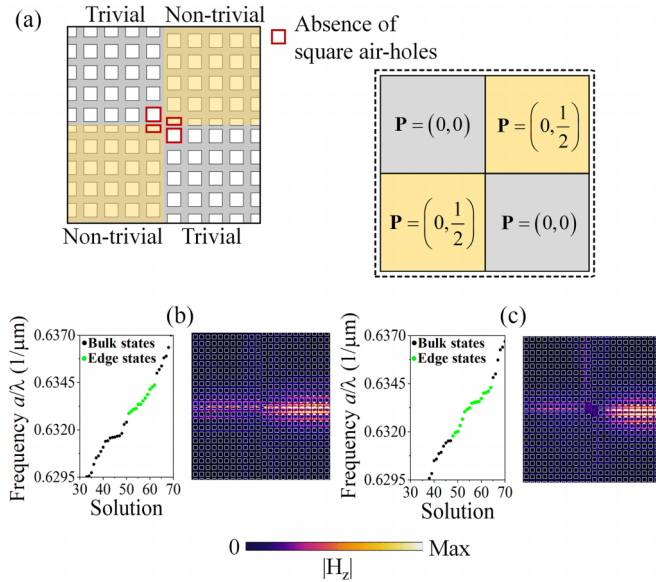


FIG. 6. Demonstration of the absence of corner-Dirac modes in a system without higher-order topology. (a) Configuration of a TBC with photonic lattices having a 2D polarization $\mathbf{P} = (0, 0)$ and $(0, 1/2)$. On the right is the distribution of 2D polarization in the TBC. (b) Solutions of the eigenfrequencies obtained close to the Dirac frequency, showing only the existence of edge states. On the right is the edge state closest to the Dirac frequency. (c) Solutions of the eigenfrequencies close to the Dirac frequency, now with the structural defect introduced in the new TBC. Likewise, we show on the right the edge state closest to the Dirac frequency.

again find only edge states which are robust to the presence of the structural defect but without the presence of confined corner states. Therefore, this paper demonstrates that for the existence of corner-Dirac states higher-order topological features are strictly necessary, in particular, the higher-order filling anomaly that produces a nonzero corner charge.

V. CONCLUSION

In summary, we have analyzed the existence of the HODSM phase in a two-dimensional photonic structure and found a corner state that exists at a Dirac point without a band gap. The HODSM phase was available to induce by lifting a fourfold degeneracy and causing a higher-order phase transition. Although the system does not display a band gap, the vanishing density of states obtained at the Dirac point between two edge bands enables effective radiation suppression, allowing the generation of a confined corner state. The new corner state inherits the properties of the Dirac modes, showing an algebraic decay described by the massless Dirac equation. Furthermore, the corner-Dirac mode is robust against aggressive disturbances, as it can exist in a localized structural defect induced in the topological corner of the photonic lattice. This localized defect increases the confinement of the corner-Dirac mode by an order of magnitude since conventional Dirac modes exist intrinsically in structural defects, adding this property to the corner state. These results demonstrate that corner states can exist in more topological phases than

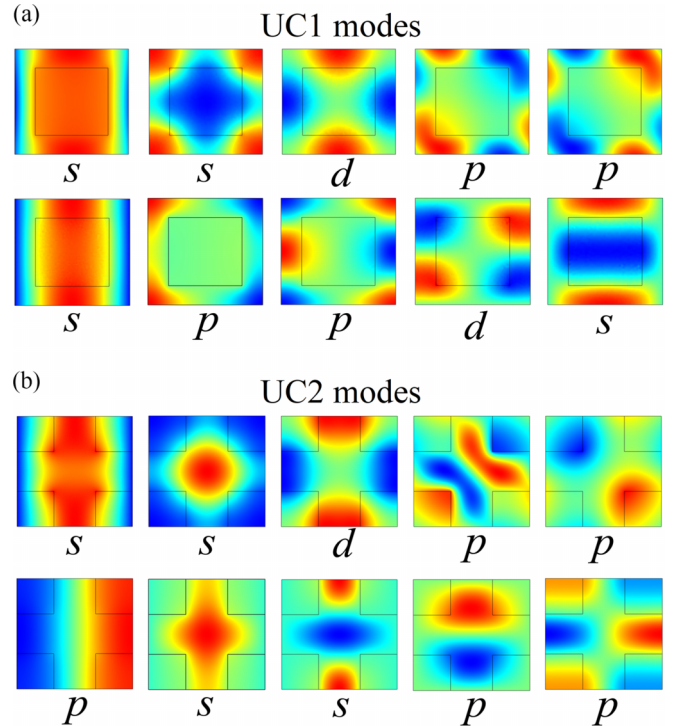


FIG. 7. Eigenmode profiles at Γ points (top panel) and X points (bottom panel) for the first five bands of unit cell UC1 in TE modes. (b) Eigenmode profiles at Γ points (upper panel) and X points (lower panel) for the first five bands of unit cell UC2 in TE modes.

previously thought and may inspire future studies in Dirac light-matter interactions.

ACKNOWLEDGMENTS

The authors want to thank Centro de Investigación en Materiales Avanzados for providing the resources required to develop this research. J.A.M.-V. and E.Y.G.-R. want to thank the Consejo Nacional de Ciencia y Tecnología for Scholarship Grants No. 866231 and No. 866214 provided to develop this research.

APPENDIX A: EIGENMODE PROFILES AT HIGH-SYMMETRY POINTS Γ AND X

The eigenmodes at the points of high symmetry Γ and X , whose parities are identified and listed in Fig. 1(e) by inversion operation, are shown in Fig. 7. These eigenmodes belong to the unit cells UC1 and UC2, and through Eq. (4) they help to determine the topological properties of the proposed photonic crystal. The five eigenmodes in the upper part of Fig. 7(a) belong to the Γ points, while the eigenmodes in the lower panels belong to the X points, both in the UC1. Subsequently, we show in Fig. 7(b) the eigenmode profiles of the first five bands, now for the case from UC2. Again, the five eigenmodes at the top correspond to the Γ points, while those at the bottom correspond to the X points. Here, one can find that the p modes have odd parity ($-$), while modes s and d have even ($+$) parity. Here, one can find that the p modes have odd parity ($-$), while modes s and d have even ($+$) parity.

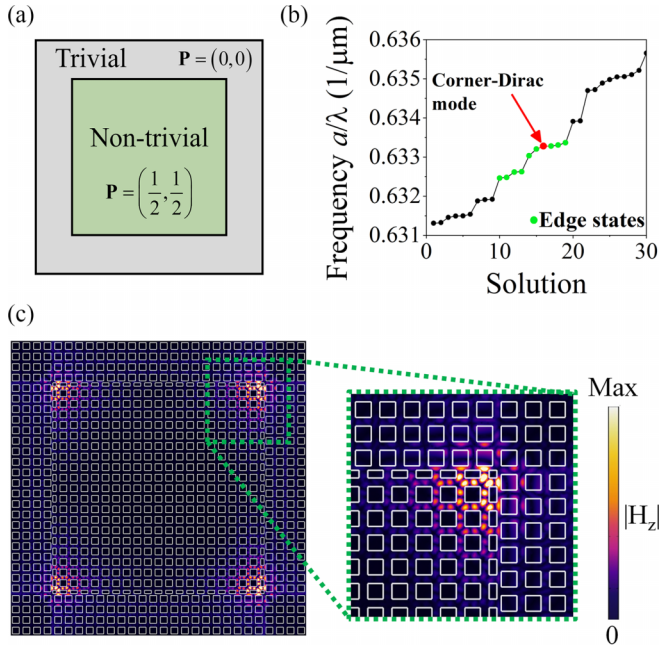


FIG. 8. (a) Conventional PhC box-shaped design. (b) Photonic eigenmodes of the topological box-shaped PhC found around the Dirac point. The red dot shows the corner-Dirac mode. (c) Field distribution corresponding to the Dirac-corner mode in the box-shaped PhC.

APPENDIX B: CORNER-DIRAC MODE IN A CONVENTIONAL DESIGN

In the literature, it is common to find a box-shaped design like the one shown in Fig. 8(a). In this type of structure, the nontrivial topology forms a square region with four corners bounded by the trivial photonic lattice. In this way, we found four corner states on each topological corner of the box-shaped PhC. Figure 8(b) shows the photonic eigenmodes with frequencies near the Dirac point in the box-shaped PhC. The frequency of the corner-Dirac mode that appears in the conventional structure is located at the Dirac frequency and has the same modal distribution as the mode found for TBC [see Fig. 8(c)]. Furthermore, the field distribution of the corner-Dirac mode is located at the four topological corners, which

confirms its origin as a corner state. This result shows that the Dirac corner mode is not a result of the TBC architecture but rather the higher-order topology of the nontrivial photonic lattice and the vanishing density of states.

APPENDIX C: LOCALIZED STRUCTURAL DEFECT MODE IN THE HIGHER-ORDER TOPOLOGICAL INSULATING PHASE

In this section, we show that a structural defect located at the topological corner of the bowtie cavity, described in the main paper, can support corner states in the HOTI phase. This study was performed to support the notion that a higher-order topological phase can support corner states in structural defects and thus contribute to justifying the existence of the corner-Dirac mode in the higher-order Dirac semimetal phase. In addition, we draw a further distinction between the corner states in the HOTI and HODSM phases, pointing out that in the HOTI phase the Q factor decreases with the structural defect while in the HODSM phase the quality factor is improved.

The structural defect considered is the same as the one shown in Fig. 2(a) in the main paper. The photonic band diagram of the UC1 and UC2 shown in Fig. 9(a) highlights the band gap with a light green rectangle. Subsequently, Fig. 9(b) shows the eigenfrequencies near the band gap and the field distribution corresponding to the corner state. In this first case, we made the calculations without the structural defect for comparative purposes. Then, the calculations made for the TBC with the addition of a structural defect are shown in Fig 9(c). In this last case of interest, we show the presence of the well-localized corner state in the defect region, and other resonant modes also arise within the band gap [see Fig. 9(c) in the eigenfrequencies panel], as expected. The corner state does not present a significant change in the modal distribution despite the presence of the structural defect. However, we see that the spectral localization does experience a slight shift, accompanied by a decrease in the quality factor Q . The Q factor value for the case without the TBC defect is 2.6×10^6 and drops to 3×10^5 when the defect is added, which is still a high Q value. This last point is important to highlight because we show in the main paper that the corner-Dirac mode confinement is enhanced by the presence of the structural defect without undergoing significant changes in the modal distribution and spectral position.

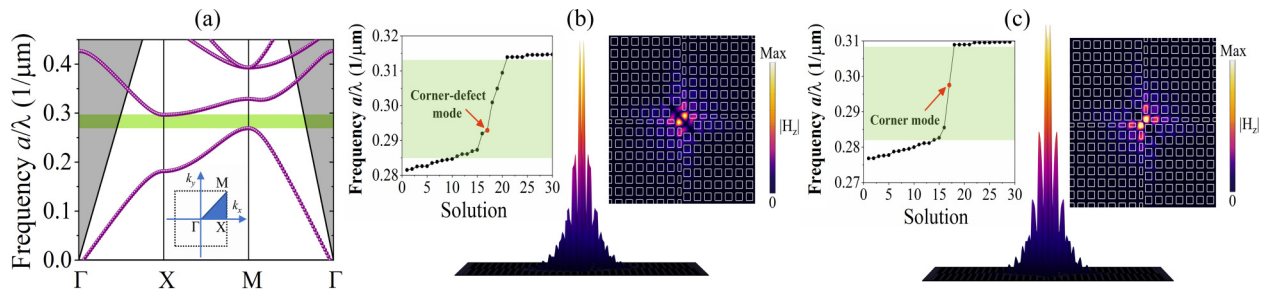


FIG. 9. Region of the photonic band structure where the HOTI phase is located. (b) Solutions of the eigenfrequencies found near the photonic gap where the corner state of the HOTI phase is located. Also, we show the distribution of the corner state field in the middle of the gap and its respective height plot. (c) Solutions of the eigenfrequencies found near the photonic gap, now with a structural defect located in the center of the TBC. The field distribution and its height plot are also shown, indicating that the corner state remains strongly confined to the topological corner of the TBC.

- [1] F. D. M. Haldane and S. Raghu, *Phys. Rev. Lett.* **100**, 013904 (2008).
- [2] R. A. Sepkhanov, Y. B. Bazaliy, and C. W. J. Beenakker, *Phys. Rev. A* **75**, 063813 (2007).
- [3] S. R. Zandbergen and M. J. A. de Dood, *Phys. Rev. Lett.* **104**, 043903 (2010).
- [4] O. Bahat-Treidel, O. Peleg, M. Grobman, N. Shapira, M. Segev, and T. Pereg-Barnea, *Phys. Rev. Lett.* **104**, 063901 (2010).
- [5] X. Zhang, *Phys. Rev. Lett.* **100**, 113903 (2008).
- [6] Y. Akahane, T. Asano, B. Song, and S. Noda, *Nature (London)* **425**, 944 (2003).
- [7] Z. Zhang and M. Qiu, *Opt. Express* **12**, 3988 (2004).
- [8] B. Song, S. Noda, T. Asano, and Y. Akahane, *Nat. Mater.* **4**, 207 (2005).
- [9] E. Kuramochi, M. Notomi, S. Mitsugi, A. Shinya, T. Tanabe, and T. Watanabe, *Appl. Phys. Lett.* **88**, 041112 (2006).
- [10] M. Notomi and H. Taniyama, *Opt. Express* **16**, 18657 (2008).
- [11] A. Simbula, M. Schatzl, L. Zagaglia, F. Alpeggiani, L. C. Andreani, F. Schäffler, T. Fromherz, M. Galli, and D. Gerace, *APL Photonics* **2**, 056102 (2017).
- [12] T. Asano, Y. Ochi, Y. Takahashi, K. Kishimoto, and S. Noda, *Opt. Express* **25**, 1769 (2017).
- [13] Y. Lai, S. Pirota, G. Urbinati, D. Gerace, M. Minkov, V. Savona, A. Badolato, and M. Galli, *Appl. Phys. Lett.* **104**, 241101 (2014).
- [14] T. Yoshie, A. Scherer, J. Hendrickson, G. Khitrova, H. M. Gibbs, G. Rupper, C. Ell, O. B. Shchekin, and D. G. Deppe, *Nature (London)* **432**, 200 (2004).
- [15] D. Englund, D. Fattal, E. Waks, G. Solomon, B. Zhang, T. Nakaoka, Y. Arakawa, Y. Yamamoto, and J. Vuckovic, *Phys. Rev. Lett.* **95**, 013904 (2005).
- [16] A. Faraon, I. Fushman, D. Englund, N. Stoltz, P. Petroff, and J. Vuckovic, *Nat. Phys.* **4**, 859 (2008).
- [17] K. Rivoire, Z. Lin, F. Hatami, W. T. Masselink, and J. Vuckovic, *Opt. Express* **17**, 22609 (2009).
- [18] A. Lyasota, C. Jarlov, M. Nyman, A. Miranda, M. Calic, B. Dwir, A. Rudra, A. Shevchenko, and E. Kapon, *Phys. Rev. X* **12**, 021042 (2022).
- [19] M. Z. Hasan and C. L. Kane, *Rev. Mod. Phys.* **82**, 3045 (2010).
- [20] N. R. Cooper, J. Dalibard, and I. B. Spielman, *Rev. Mod. Phys.* **91**, 015005 (2019).
- [21] T. Ozawa, H. M. Price, A. Amo, N. Goldman, M. Hafezi, L. Lu, M. C. Rechtsman, D. Schuster, J. Simon, O. Zilberberg, and I. Carusotto, *Rev. Mod. Phys.* **91**, 015006 (2019).
- [22] L.-H. Wu and X. Hu, *Phys. Rev. Lett.* **114**, 223901 (2015).
- [23] Y. Ota, F. Liu, R. Katsumi, K. Watanabe, K. Wakabayashi, Y. Arakawa, and S. Iwamoto, *Optica* **6**, 786 (2019).
- [24] B.-Y. Xie, H.-F. Wang, H.-X. Wang, X.-Y. Zhu, J.-H. Jiang, M.-H. Lu, and Y.-F. Chen, *Phys. Rev. B* **98**, 205147 (2018).
- [25] X. Zhang, H.-X. Wang, Z.-K. Lin, Y. Tian, B. Xie, M.-H. Lu, Y.-F. Chen, and J.-H. Jiang, *Nat. Phys.* **15**, 582 (2019).
- [26] A. Shi, B. Yan, R. Ge, J. Xie, Y. Peng, H. Li, W. E. I. Sha, and J. Liu, *Opt. Lett.* **46**, 1089 (2021).
- [27] M. Serra-Garcia, V. Peri, R. Süssstrunk, O. R. Bilal, T. Larsen, L. Guillermo-Villanueva, and S. D. Huber, *Nature (London)* **555**, 342 (2018).
- [28] C. W. Peterson, W. A. Benalcazar, T. L. Hughes, and G. Bahl, *Nature (London)* **555**, 346 (2018).
- [29] S. Imhof, C. Berger, F. Bayer, J. Brehm, L. W. Molenkamp, T. Kiessling, F. Schindler, C. H. Lee, M. Greiter, T. Neupert, and R. Thomale, *Nat. Phys.* **14**, 925 (2018).
- [30] W. A. Benalcazar, J. C. Y. Teo, and T. L. Hughes, *Phys. Rev. B* **89**, 224503 (2014).
- [31] W. A. Benalcazar, B. A. Bernevig, and T. L. Hughes, *Science* **357**, 61 (2017).
- [32] W. A. Benalcazar, B. A. Bernevig, and T. L. Hughes, *Phys. Rev. B* **96**, 245115 (2017).
- [33] Z. Song, Z. Fang, and C. Fang, *Phys. Rev. Lett.* **119**, 246402 (2017).
- [34] J. Langbehn, Y. Peng, L. Trifunovic, F. von Oppen, and P. W. Brouwer, *Phys. Rev. Lett.* **119**, 246401 (2017).
- [35] F. Schindler, A. M. Cook, M. G. Vergniory, S. S. P. Parkin, Z. Wang, B. A. Bernevig, and T. Neupert, *Sci. Adv.* **4**, eaat0346 (2018).
- [36] O. Zilberberg, S. Huang, J. Guglielmon, M. Wang, K. P. Chen, Y. E. Kraus, and M. C. Rechtsman, *Nature (London)* **553**, 59 (2018).
- [37] B. J. Wieder and B. A. Bernevig, [arXiv:1810.02373](https://arxiv.org/abs/1810.02373).
- [38] G. van Miert and C. Ortix, *Phys. Rev. B* **98**, 081110(R) (2018).
- [39] M. Ezawa, *Phys. Rev. B* **98**, 045125 (2018).
- [40] W. A. Benalcazar, T. Li, and T. L. Hughes, *Phys. Rev. B* **99**, 245151 (2019).
- [41] E. Lee, R. Kim, J. Ahn, and B.-J. Yang, *npj Quantum Mater.* **5**, 1 (2020).
- [42] X.-L. Sheng, C. Chen, H. Liu, Z. Chen, Z.-M. Yu, Y. X. Zhao, and S. A. Yang, *Phys. Rev. Lett.* **123**, 256402 (2019).
- [43] F. Schindler, M. Brzezińska, W. A. Benalcazar, M. Iraola, A. Bouhon, S. S. Tsirkin, M. G. Vergniory, and T. Neupert, *Phys. Rev. Res.* **1**, 033074 (2019).
- [44] I. Petrides and O. Zilberberg, *Phys. Rev. Res.* **2**, 022049(R) (2020).
- [45] H.-R. Kim, M.-S. Hwang, D. Smirnova, K.-Y. Jeong, Y. Kivshar, and H.-G. Park, *Nat. Commun.* **11**, 5758 (2020).
- [46] W. X. Zhang *et al.*, *Light.: Sci. Appl.* **9**, 109 (2020).
- [47] A. Cerjan, M. Jürgensen, W. A. Benalcazar, S. Mukherjee, and M. C. Rechtsman, *Phys. Rev. Lett.* **125**, 213901 (2020).
- [48] W. A. Benalcazar and A. Cerjan, *Phys. Rev. B* **101**, 161116(R) (2020).
- [49] Z.-G. Chen, C. Xu, R. AlJahdali, J. Mei, and Y. Wu, *Phys. Rev. B* **100**, 075120 (2019).
- [50] K. Xie, H. Jiang, A. D. Boardman, Y. Liu, Z. Wu, M. Xie, P. Jiang, Q. Xu, M. Yu, and L. E. Davis, *Laser Photon. Rev.* **8**, 583 (2014).
- [51] Q. Mao, L. Hu, G. Ding, and K. Xie, *Opt. Commun.* **503**, 127449 (2022).
- [52] Q. Mao, K. Xie, L. Hu, Q. Li, W. Zhang, H. Jiang, Z. Hu, and E. Wang, *Appl. Opt.* **55**, B139 (2016).
- [53] Q. Mao, K. Xie, L. Hu, Q. Li, W. Zhang, H. Jiang, Z. Hu, and E. Wang, *Opt. Commun.* **384**, 11 (2017).
- [54] A. González-Tudela and J. I. Cirac, *Phys. Rev. A* **97**, 043831 (2018).
- [55] J. Perczel and M. D. Lukin, *Phys. Rev. A* **101**, 033822 (2020).
- [56] B. A. Bernevig, *Nat. Phys.* **11**, 698 (2015).
- [57] A. Burkov, *Nat. Mater.* **15**, 1145 (2016).

- [58] C. Fang, L. Lu, J. Liu, and L. Fu, *Nat. Phys.* **12**, 936 (2016).
- [59] M. Lin and T. L. Hughes, *Phys. Rev. B* **98**, 241103(R) (2018).
- [60] B. J. Wieder, Z. Wang, J. Cano, X. Dai, L. M. Schoop, B. Bradlyn, and B. A. Bernevig, *Nat. Commun.* **11**, 627 (2020).
- [61] H. Qiu, M. Xiao, F. Zhang, and C. Qiu, *Phys. Rev. Lett.* **127**, 146601 (2021).
- [62] Q. Wei, X. Zhang, W. Deng, J. Lu, and S. Jia, *Nat. Mater.* **20**, 812 (2021).
- [63] Z. Wang, D. Liu, H. T. Teo, Q. Wang, H. Xue, and B. Zhang, *Phys. Rev. B* **105**, L060101 (2022).
- [64] S. Vaidya, W. A. Benalcazar, A. Cerjan, and M. C. Rechtsman, *Phys. Rev. Lett.* **127**, 023605 (2021).
- [65] Y. Chen, F. Meng, Z. Lan, B. Jia, and X. Huang, *Phys. Rev. Appl.* **15**, 034053 (2021).
- [66] J. A. Medina-Vázquez, J. G. Murillo-Ramírez, E. Y. González-Ramírez, and S. F. Olive-Méndez, *J. Appl. Phys.* **132**, 133104 (2022).
- [67] M. Li, D. Zhirihin, M. Gorlach, X. Ni, D. Filonov, A. Slobozhanyuk, A. Alù, and A. B. Khanikaev, *Nat. Photonics* **14**, 89 (2020).
- [68] X.-T. He, M.-Y. Li, H.-Y. Qiu, W.-S. Ruan, L.-D. Zhou, L. Liu, X.-D. Chen, W.-J. Chen, F.-L. Zhao, and J.-W. Dong, *Photon. Res.* **9**, 1423 (2021).
- [69] L. He, Z. Addison, E. J. Mele, and B. Zhen, *Nat. Commun.* **11**, 3119 (2020).